Available online at www.sciencedirect.com

ScienceDirect

Journal of Sound and Vibration 317 (2008) 30–49

JOURNAL OF SOUND AND VIBRATION

www.elsevier.com/locate/jsvi

Experimental characterization and modeling of microsliding on a small cantilever quartz beam

H. Nouira[a,*], E. Foltête[b], B. Ait Brik[b], L. Hirsinger[b], S. Ballandras[c]

[a]*Laboratoire de Mécanique de Lille (LML-CNRS), Ecole Centrale de Lille, Cité Scientifique—BP 48,cité scientifique, 59651 Villeneuve d'Ascq Cedex, France*

[b]*Laboratoire de Mécanique Appliquée Raymond Chaléat (LMARC-CNRS), Institut de FEMTO-ST, 24 Chemin de l'Epitaphe, 25000 Besançon, France*

[c]*Laboratoire de Physique et Métrologie des Oscillateurs (LPMO-CNRS), Institut de FEMTO-ST, 32 Avenue de l'Observatoire, F-25044 Besançon, France*

Received 16 August 2007; received in revised form 3 March 2008; accepted 12 March 2008
Handling Editor: M.P. Cartmell
Available online 12 May 2008

Abstract

The design of mechanical systems requires various studies in order to ensure an optimal behavior during operation. In particular, the study of its dynamic behavior makes it possible to evaluate the role of a connection in the energy dissipation mechanisms. In this context, an experimental setup dedicated to small structures has been developed to quantify damping due to microsliding at the beam–clamp interface. The mechanical characterization of the clamped connection is carried out by experimental dynamic tests on a free-clamped structure. The instantaneous frequencies and damping are identified by the wavelet transform technique of a slightly nonlinear system. In parallel, numerical prediction of the equivalent damping is achieved thanks to the implementation of the regularized Coulomb law in a finite element model. A genetic algorithm and artificial neural networks are used to update the stiffness parameter and the friction coefficient. The optimized model is in good agreement with experimental results. It allows for determining the spatial distribution of microsliding and tangential force along the contact interface. The dissipated energy and equivalent damping are finally deduced according to the dynamic deflection of the free part of the beam.

---

1. Introduction

There has been growing interest in microsystem research these last years, especially for the domain of energy harvesting [1–3]. For that purpose, many solutions have been proposed based on structures vibrating at frequencies low enough to ease their excitation by ambient (very low frequency) solicitations. However, less work has been performed in optimizing the embedment of such energy converters and to minimizing energy losses due to friction at clamping areas. This work lies within the general scope of the study and design of a microconverter (volume $<100\,\text{mm}^3$) of mechanical vibratory energy (usually available in great quantity in the

---

[*] Corresponding author. Tel.: +33 3 20 33 53 44.
E-mail address: hhichem.nouira@ec-lille.fr (H. Nouira).

0022-460X/$ - see front matter © 2008 Elsevier Ltd. All rights reserved.
doi:10.1016/j.jsv.2008.03.017

environment of some sensor) for electric power by through the use of piezoelectric materials. The use of this microconverter is designed to replace batteries that are source of pollution. Moreover, the replacement of batteries can be difficult due to limited accessibility within a structure.

The previous architecture of the microconverter is composed of a silicon beam fixed by adhesive material (epoxy resin (SU8) or compressed gold) between four piezoelectric plates (quartz or lithium of niobate) in the fitting region. The unit is then clamped by screws between the rigid supports 1 and 2 as shown in Fig. 1. The excitation of the support 1 introduces the vibrations of the free part of the microconverter, which deforms the piezoelectric plates. The cyclic deformation energy is then converted to the electrical energy using an associate electronic system. In order to obtain a good energy transformation, minimal energy losses are required. In this context, various dissipation processes can be observed in a vibrating structure. The internal dissipation, due to molecular diffusion and mutual movements within the body of the device [4,5], is relatively weak for metals and single-crystal materials at our operating frequencies (a few kHz) and its effect can be neglected [6]. Thermoelastic dissipation results from a coupling between the mechanical behavior of the material and thermodynamic principles and results in a considerable dissipation process [7,8]. The free-clamped beam vibration in contact with squeeze air and airflow also can generate considerable viscous damping causing significant energy dissipation [9–12]. Also, when a cantilever beam vibrated in open air, a part of the elastic energy trapped in the environment is converted to acoustic radiation at each vibration cycle, reducing the quality factor of the whole system. This can be accounted for by an appropriate simulation of the fluid medium's influence on the vibrating structure, for instance coupling a Green's function representation of the open medium contribution to the localized vibration via boundary element methods [13]. The vibration of an assembled structure by a bolt enables the phenomenon of friction because interfaces in contact are never perfectly smooth and contain irregularities, like asperities, even if the materials are carefully polished [14]. The application of a tightening torque amount introduces a normal force on the whole contact asperities [15]. When structures vibrate, resistance to microsliding originates from interactions between asperities where energy dissipation phenomena occur as heat dissipation during the different steps of formation and separation of microcontacts. At the scale of contact microgeometry, the microsliding phenomenon results in three principal stages where the first can be decomposed in an elastic strain, followed by a plastic deformation accompanied by an interpenetration of the asperities. An adhesive connection takes place in a second stage. In the third stage the shearing of the junctions occurs, followed by an elastic relaxation of the asperities [16]. The higher microsliding effect corresponds to the higher dissipated energy. Such phenomena result in weak quality factors of the beam vibration defined as the rate between the restored and reported energies of the structure by one cycle of vibration [17].

The computation of dissipated energy due to the stick-slip phenomenon requires the evaluation of relative displacements at the contact interface as well as the corresponding tangential force [18]. The analysis of the energy dissipation is generally based on the constitutive physics models related to the interfaces, enabling representation of the structure behavior in a local way, or based on phenomenological models deduced from experimental observations [19]. According to the friction force function, two types of friction models are generally defined. The first is known as a static friction model and it is based on the assumption that the relative speed of the surfaces in contact is constant [20]. The second type of friction models is known as

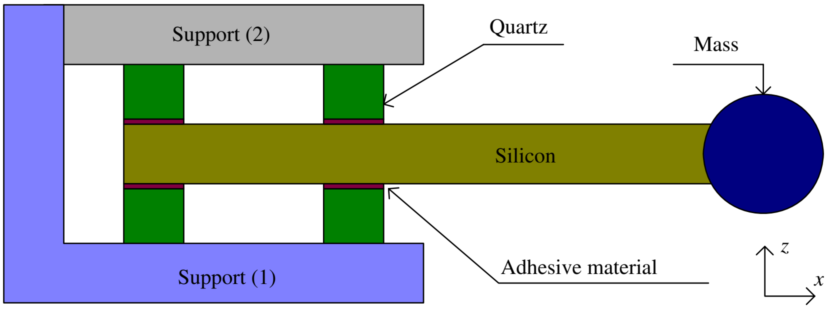

Fig. 1. Scheme of the microconverter.

dynamic model, in which the equations are based on the internal state variables [21]. In that matter, Iwan proposed phenomenological models based on spring wiper elements known as Jenkins or Masing elements [22–24]. Olofsson [25] proposed an analytical model based on the Hertz theory, with the aim of computing dissipated energy caused by the stick-slip phenomenon.

The assembly between silicon and the piezoelectric plates is very rigid and advantages the low energy dissipation. However, the screw fixation of the microconverter between the supports 1 and 2 (contact between piezoelectric plates and supports 1 and 2) is very delicate to perform because of the fragility of the employed material (silicon and quartz). In this paper, the experimental tests on the first bending mode of a small cantilever quartz beam have been performed in order to study this specific problem of connection by screws and especially the contact between the quartz and the support. Then, the study of the interface contact between the quartz and the support aims to quantify the dissipated energy and to the technological choice of the final architecture of the microconverter. The beam system is excited by burst sine force. The analysis of the recorded signal is carried out by the wavelet transform identification technique with complex values [26–28]. Therefore, the wavelet transform amplitude of a slightly nonlinear system is related to the modal equivalent damping coefficients, and the phase is related to the eigen-value coefficients of the considered mode [29]. This technique of identification was also developed by Heller [19] in order to characterize bolted structures on large scales, based on the general modified Morlet wavelet. Instantaneous parameters can be identified according to the structure vibration amplitude.

The second part of this paper is dedicated to the modeling of the modal equivalent damping coefficient based on the phenomenological models of Iwan [22] using the regularized Coulomb law. An optimization step is employed based on twin genetic algorithms (GAs) with a neuron network [30,31] in order to reduce computation delays. From the optimized modeling, the tangential force and microsliding are obtained allowing for the prediction of dissipated energy and modal equivalent damping at the beam fitting.

2. Experimental study

The experiment is defined to emphasize the influence of microsliding produced at the clamped part of a quartz cantilever polished on one side and lapped on the other side. The average arithmetic depth of the roughness measured by a microprofilometer is equal to 3×10^{-8} m on the polished surface and to 2.1×10^{-7} m on the lapped one. It should also be noticed that the roughness changes slightly along the surface. The dimension of the quartz structure is equal to $0.36 \times 3.6 \times 15\,\mathrm{mm}^3$. This specimen is clamped by an aluminum clamping system, consisting of two plates with a notch (Fig. 2). The average arithmetic depth of the roughness of aluminum plate is equal to 5×10^{-7} m. The thickness of the quartz beam is negligible compared to the thickness of each plate (5 mm). The notch jams the quartz beam movement in the y-axis direction. The assembly of the two plates together with the beam is very carefully achieved over a beam length of 7.2 mm by four screws (using a torque wrench) in order to obtain uniform distribution of normal force over the contact.

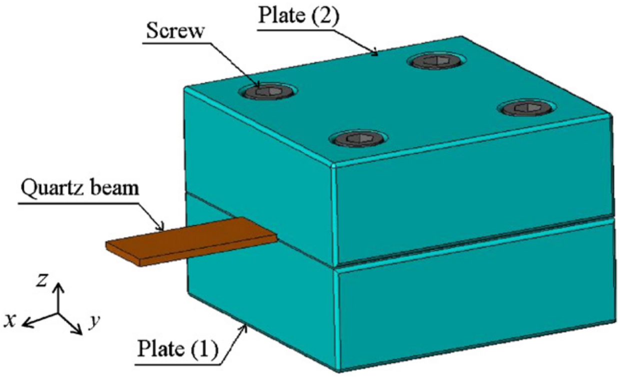

Fig. 2. The 3D diagram of the clamped quartz beam.

When the clamp is too high or excessive and the normal force non-uniform, the quartz beam can be immediately damaged.

The first plate is fixed on the electrodynamic shaker (Brüel and Kjaer (B&K)), used in the vertical position, and the second carries an accelerometer (Fig. 3). The whole setup, including the electrodynamic shaker, the support system, the beam and the accelerometer is placed in a lined enclosure and upholstered using foam. A tight borosilicate porthole is used as a lid. It ensures the transmission of approximately 90 percent of a general wave whose amplitude varies between 4 and 7×10^{-7} m. The enclosure is connected to a vacuum pump in order to create a primary vacuum monitored by a pressure gauge. The time-dependent response of the beam is recorded by using a contactless method of the Doppler vibrometer, which is focused on the free-end of the cantilever quartz beam that is cleaned with ethanol before measurements. Since quartz is transparent material, a thin aluminum layer is sputtered with a very weak surface roughness (<1 nm) on the top face. Typically, it is a physical vapor deposition (PVD) surface made of spherical aluminum aggregates whose diameter is about 10–50 nm. The aluminum layer ensures well the reflection of the laser beam in order to record the velocity amplitude of the free-end beam vibration. The quartz cantilever is first excited by a harmonic force near one of its resonance frequencies and the free response is recorded by stopping excitation signal. The free response of

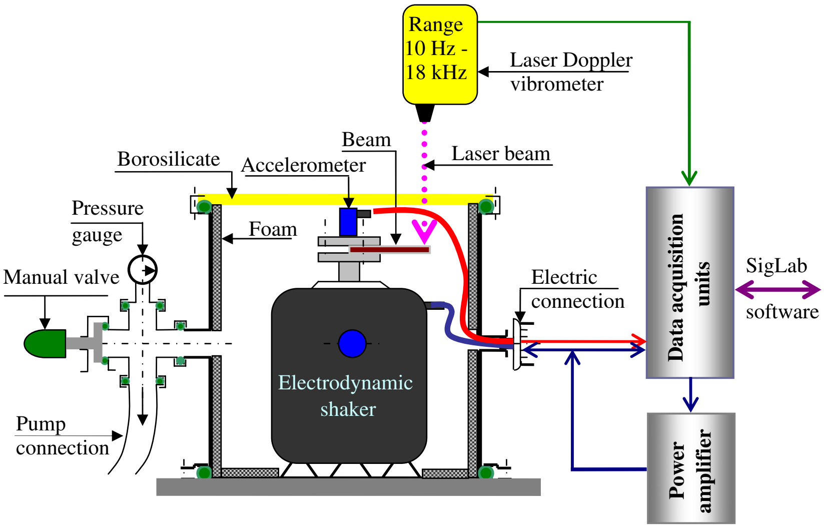

Fig. 3. Explanatory experiment diagram.

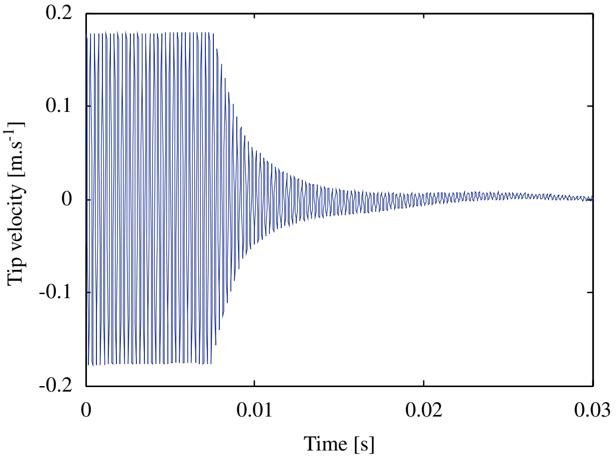

Fig. 4. Tip velocity of the free end of the cantilever beam versus time.

the vibrating structure on its first eigen-mode is then acquired (Fig. 4). The acquisition and signal generation are carried out by a multichannel dynamic signal analyzer (SigLab).

3. Nonlinear identification from the free responses

The dynamic behavior of a slightly nonlinear system results in a strong dependence of the frequencies and damping on the amplitude of vibration of the structure. On the other hand, the dynamic behavior for constant response amplitude is often assumed to be linear. Sine stepping measurements can thus be carried out with a constant amplitude response for a set of selected amplitudes. For each measurement, a linear identification technique provides the characteristics of the model associated with the given amplitude of vibration. In this way, a discrete description of the nonlinear dynamic behavior is obtained. The major disadvantage of this method is the long measurement time necessary for a relatively small quantity of information. Recently, a time-frequency approach for free responses was developed [11,29,32]. It has the advantage of providing a quasi-continuous description of the parameters (instantaneous frequency and damping as well as equivalent modal frequency and damping) from only one time response. The principle is simple and is based on treating the free response of the structure like the response of a nonlinear oscillator with only one degree of freedom. This response makes it possible to sweep a whole range of amplitudes in only one measurement. The continuous wavelet transform (CWT) of the recorded signal is then calculated and used to identify the instantaneous frequency and damping.

3.1. Continuous wavelet transform (CWT)

The CWT can be explained by analogy with the Fourier transform. In both cases, the considered signal is represented by a linear combination of basic functions. For the Fourier transform, the basic functions are trigonometric functions covering the entire considered time interval, more or less dilated by a frequency parameter. For the CWT, the basic functions are deduced from a reference function, called the mother wavelet, defined in time and allowing the description of the signals for a localized frequency. A very common mother wavelet is the general modified Morlet wavelet:

$$\Psi(t) = \mathrm{e}^{(\mathrm{j}\omega_0 t)}\,\mathrm{e}^{-t^2/N} \tag{1}$$

where ω_0 is the wavelet frequency and N is the parameter which controls the shape of the basic wavelet ($N>0$). The dilated Fourier transform version of the modified Morlet wavelet is presented in the following:

$$\hat{\Psi}(\omega) = \mathrm{e}^{N/4(\omega-\omega_0)^2} \tag{2}$$

An important value of N gives a narrower spectrum allowing a better frequency resolution. The optimal value of N is obtained by minimizing the entropy of the wavelet coefficient (see Ref. [33] for more details). The CWT gives time and frequency information about the analyzed data. The basis functions are deduced from the Morlet mother wavelet, which is dilated by a scale parameter u defining the size of analyzing window and localized in the time domain by a position parameter v:

$$\Psi_{(v,u)}(t) = \frac{1}{\sqrt{u}}\Psi\left(\frac{t-v}{u}\right) \tag{3}$$

The CWT of a temporal signal $x(t)$ at the scale u and at the position v is calculated by correlating with the corresponding wavelet [27]:

$$T_x^{\Psi}(u,v) = \frac{1}{\sqrt{u}}\int_{-\infty}^{+\infty} x(t)\overline{\Psi\left(\frac{t-v}{u}\right)}\,\mathrm{d}t \tag{4}$$

where $\bar{\Psi}$ is the complex conjugate of $\Psi(t)$. The skeleton of the CWT is the modulus of the CWT coefficient $|T_x(u,v)|$ that represents a surface in the time-frequency space (Fig. 5(a)). The ridge of the CWT is the locus $(u_r(v),v)$ of local maxima on the CWT skeleton, which is described by Eq. (5) and represented in Fig. 5(b).

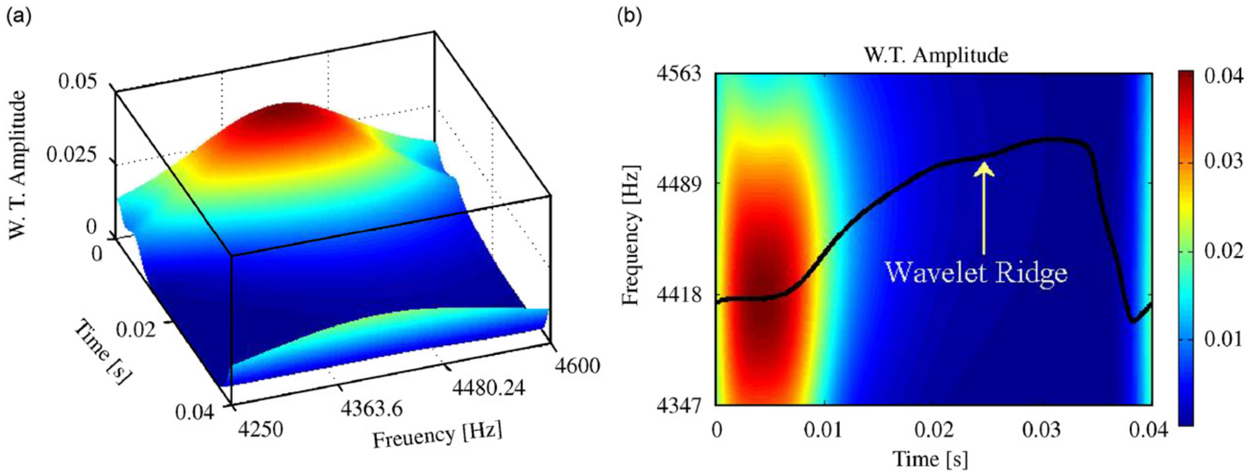

Fig. 5. (a) Continuous wavelet transform amplitude for the free response and (b) ridge of resonance frequency versus time.

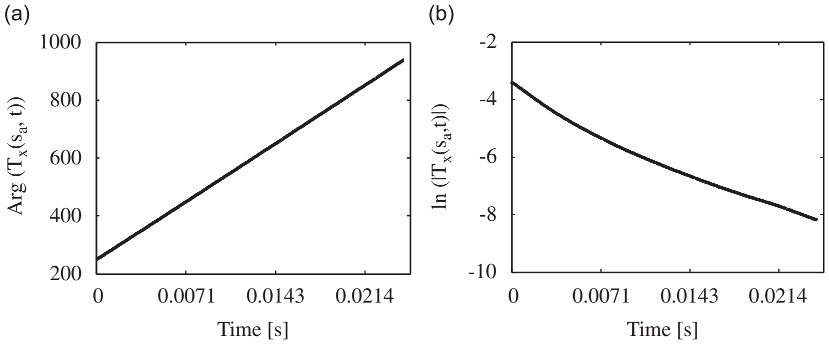

Fig. 6. (a) Argument of the continuous wavelet transform and (b) logarithm edge of the continuous wavelet transform.

For more details, see Ref. [33]:

$$|T_x(u_r(v),v)| = \max_u(|T_x(u,v)|) \tag{5}$$

3.2. Identification of equivalent modal parameters

By using the theory of asymptotic signals [34], a slightly nonlinear oscillator can be characterized by its equivalent modal frequency $\omega_e(a)$ and damping $\xi_e(a)$, where the parameter a denotes the amplitude of vibration. These two parameters can be identified thanks to the CWT. A brief discussion of the major issues of the procedure is given in Heller [19]. The first step consists in computing the CWT of the resonator free response and locating its ridge. It has been shown that the resonator instantaneous frequency is equal to the time derivative of the argument of the CWT ridge (Fig. 6(a)):

$$\omega_e(v) = \frac{\mathrm{d}}{\mathrm{d}v}\mathrm{Arg}[T_x(u_r(v),v)] \tag{6}$$

The instantaneous damping coefficient is obtained from the logarithmic decrement of the modulus of the CWT ridge (Fig. 6(b)):

$$\zeta_e(v) = -\frac{1}{\omega_0}\frac{\mathrm{d}\ln(|T_x(u_r(u),v)|)}{\mathrm{d}v} \tag{7}$$

where ω_0 is the natural angular frequency of the undamped system. The second step consists in identifying the envelope of the signal. In our case, the measurements were achieved using a laser vibrometer. It was thus necessary to integrate the signal in order to obtain a displacement envelope. Finally, the equivalent modal frequency and damping are obtained by combining the instantaneous parameters and the envelopes. Note that the natural angular frequency ω_0 is equal to $\omega_e(a = 0)$ and is obtained by an extrapolation of $\omega_e(a)$ for a small amplitude range. It also must be stated that the beginning and the end of the modulus of the CWT cannot be used because of edge effect [28,35]. Note that the edge effect can be reduced by adding zeros or by adding negative values of the signal at the beginning and the end of the signal.

3.3. Dynamic release tests results

The identification method of the nonlinear parameters from dynamic recordings of release tests is applied to the assembled device (the clamped cantilever quartz beam and its embedding) presented previously. Both experimental quantification uncertainties and influence of the ambient air pressure variation between the primary vacuum and the atmospheric pressure inside the enclosure are basically studied and presented by Nouira et al. [11]. In this paper, only the results performed under primary vacuum condition corresponding to the first vibration mode are reported. The time-frequency approach for a free response has the advantage of providing a quasi-continuous parameter description starting from a time-domain measurement. The results of the nonlinear analysis of the dynamic release response show the time evolution of the instantaneous frequencies and damping, respectively (Figs. 7(a) and (b)). The evolution of the equivalent modal frequency (Fig. 7(c)) and damping (Fig. 7(d)) versus the deflection of the free part of the beam are deduced from the instantaneous parameters by using the signal envelope.

The identified modal frequencies and the modal equivalent damping emphasize nonlinear effects, demonstrating that the dynamic behavior depends on the deflection of the clamped structure. The evolution of the frequency can be decomposed into two different parts: first the frequency increases linearly, and then it

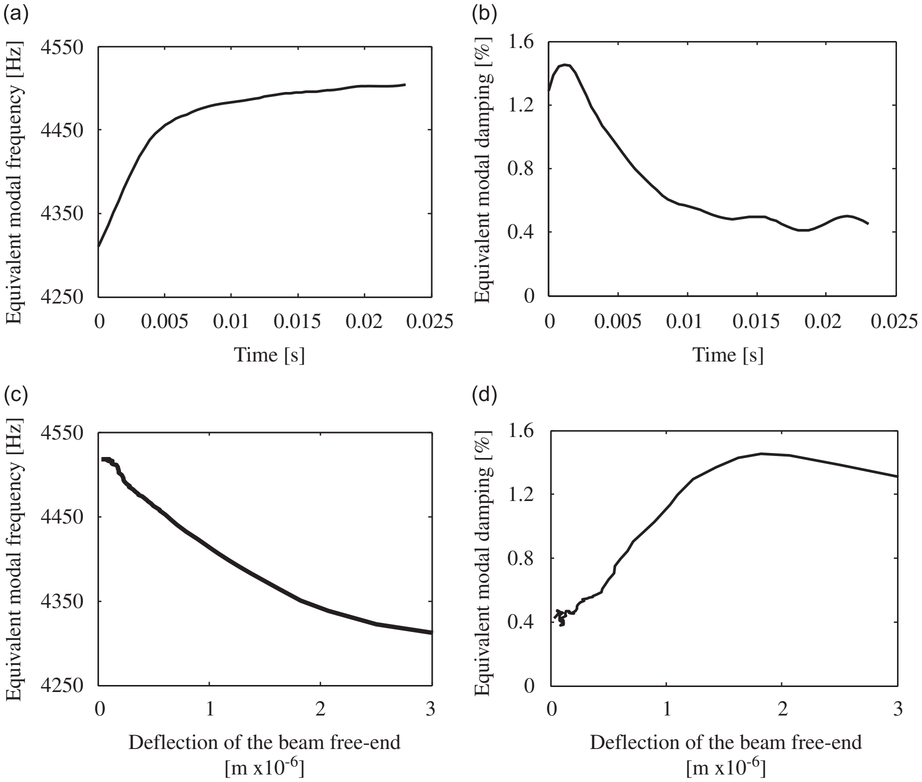

Fig. 7. (a) Instantaneous frequency, (b) instantaneous damping, (c) equivalent modal frequency and (d) equivalent modal damping.

tends to become stable. The evolution of equivalent modal damping also exhibits the presence of two sections: first the damping increases, then it decreases slowly. The maximum value of 1.46 percent is observed at $t = 0.002$ s. The corresponding quality factor for this supported structure is rather small (~35). This typical behavior is very similar to the one observed on a large scale assembled structure [19], on which it has been shown that the principal dissipation is the one produced by the stick-slip effect between contact interfaces. The experimental study of the influence of the magnitude of the normal force is very difficult to perform with small quartz structure because this kind of structure is very fragile. Though the influence of the normal force magnitude is well studied on the macrostructure by Heller [19], we conclude that the contact friction in the interface is also responsible for most of the energy dissipation in our case. In order to confirm this last conclusion, a finite element model of contact based on the regularized contact law is proposed in the next section.

4. Friction modeling

Friction is the tangential reaction force between two surfaces in contact. Physically, these reaction forces are the results of many different mechanisms, which depend on the contact geometry and topology, on the properties of the bulk and surface materials of the bodies, on the displacement and relative velocity of the bodies and on the presence of lubrication. In dry sliding, the contacts between surfaces can be modeled as elastic and perfect plastic deformation forces of microscopical asperities in contact, see Refs. [36,37]. The friction force is basically electromagnetic: the atoms of one surface "stick" to atoms of the other (adhesive junction) just before snapping apart (Fig. 8), causing the atomic vibrations, and thus transforming the work needed to maintain the sliding into heat.

Each asperity carries a p_{ns} part of the normal load P_n. If we assume a perfect plastic deformation of the asperities until the contact area of each junction has grown enough to carry its part of the normal load, the contact area junction is $\alpha_i = p_{ns}/H$, where H is the hardness of the weakest bulk material of the bodies in contact. The total contact area can thus be written as $A_c = P_n/H$. This relation holds even with an elastic junction area growth, which means that H is adjusted properly. For each asperity contact the tangential deformation is elastic until the applied shear pressure exceeds the shear strength τ_y of the surface materials, when it becomes plastic. In sliding, the friction force is thus $P_t = \tau_y A_c$, and the friction coefficient $\mu = P_t/P_n = \tau_y/H$. The friction coefficient does not depend on the normal load or the velocity in this case. Consequently, it is possible to manipulate the friction characteristics by deploying surface films of suitable materials on the bodies in contact. These surface films can also be the result of contamination or oxidation of the bulk material. The measured rough surfaces of the quartz beam and the aluminum support change slightly,

(a)

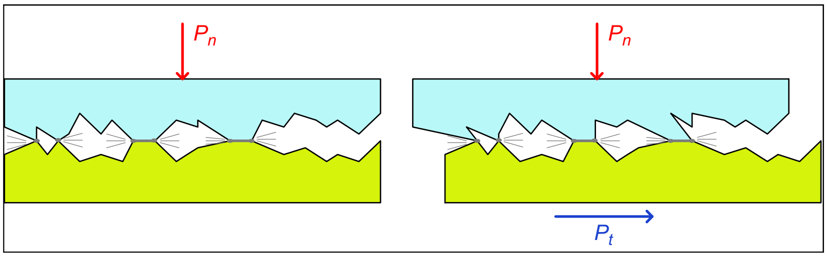

(b)

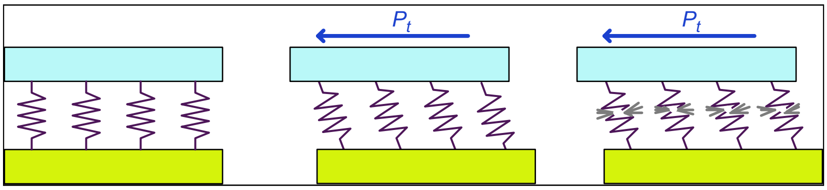

Fig. 8. (a) Metal contact between asperities and (b) visualization of breakaway.

then the friction coefficients are constant. Since the roughness of the upper and lower contact surfaces of the quartz beam is different, the friction coefficient linked to the upper and lower interfaces between the quartz beam and the aluminum support varies and increases when the roughness is higher [38].

As conclusion, it is imperative to control the modeling of the interface behavior in order to build a reliable model of the assembled structures. Fig. 9 shows a drawing of beam 2 clamped between two supports 1 and 3. Notations F, P_n, $P_t^{j\to i}$ and v_{ij} represent, respectively, the excitation force, the normal force on the interface, the tangential force applied to the solid i and the relative velocity of the solid i with respect to the solid j.

4.1. Coulomb friction

Although a lot of different models are proposed to describe the friction phenomenon, the simple and very well-known Coulomb friction will be used here. It belongs to the family of static models. The Coulomb law defines the friction force P_t according to the friction coefficient μ and to the normal force P_n (Eq. (8)). The basic principle of this model is schemed in Fig. 10(a):

$$P_t^{j\to i} = \mu|P_n|\mathrm{sgn}(v_{ij}) \tag{8}$$

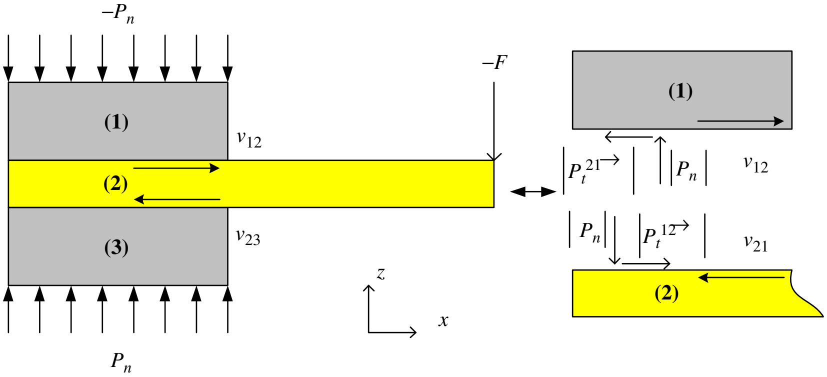

Fig. 9. Explanatory diagram of the friction phenomenon.

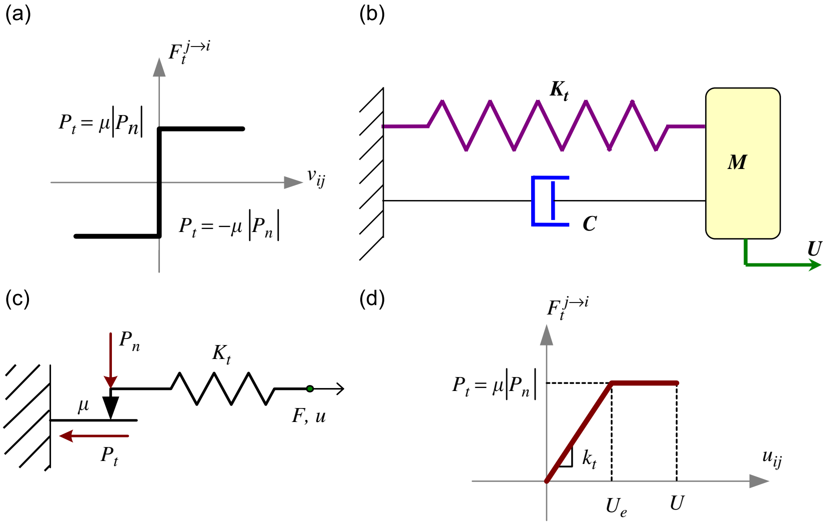

Fig. 10. (a) Description of the Coulomb law, (b) viscously damped single degree of freedom system, (c) the Prandtl model and (d) description of the regularized Coulomb law.

4.2. Equivalent damping coefficient of nonlinear systems

The energy parameters in vibrating clamped cantilever beam incorporate the influence of both strength and deformation and they include the effect of duration of strong vibrating motion. For an elastic perfectly plastic system the input energy is dissipated as hysteretic energy and kinetic energy, amongst which the major part is hysteretic energy. The concept of equivalent viscous damping was first proposed by Jacobsen [39]. Consider a viscously damped linear system [40,41] as shown in Fig. 10(b). The rate of change of energy with time ($\mathrm{d}\Delta E/\mathrm{d}t$) is given by

$$\frac{d\Delta E}{\mathrm{d}t} = F\vartheta = -C\vartheta^2 = -C\left(\frac{\mathrm{d}U(t)}{\mathrm{d}t}\right)^2 \tag{9}$$

The negative sign in equation denotes the energy dissipated with time. Assume a simple harmonic motion as $U(t) = U\sin(\omega t)$, where U is the amplitude of motion and ω is the excitation pulsation. The damping energy dissipated in a complete cycle is given by

$$\Delta E = \int_{t=0}^{2\pi/\omega} C\left(\frac{\mathrm{d}U(t)}{\mathrm{d}t}\right)^2 \mathrm{d}t = \int_{t=0}^{2\pi} CU\omega\cos^2(\omega t)\,\mathrm{d}(\omega t) = \pi\omega CU^2 \tag{10}$$

Consider the modal equivalent damping of nonlinear systems as $\xi_e = C/2M\Omega$ (where Ω is the eigen-pulsation and equal to $\Omega = (K_t/M)^{0.5}$), the ratio of energy dissipated in viscous damping to the total input energy is as specific damping capacity of structure. The total energy of the system E_e can be expressed either as the maximum potential energy $0.5KU^2$ or as the maximum kinetic energy ($0.5M\,\vartheta^2_{\max} = 0.5M\omega^2U^2$), the two being approximately equal for small values (i.e. <10 percent) of damping. Thus, equating the ratio of hysteretic energy to total input energy of elastoplastic structure to ratio of damping energy to the strain energy of linearly elastic damped structures we get

$$\Delta E(U) = 2\pi\zeta_e\frac{\omega}{\Omega}K_tU^2 = 4\pi\zeta_e\frac{\omega}{\Omega}E_e(U) \tag{11}$$

From Eq. (11), the equivalent damping coefficient is obtained and depends on the ratio between the dissipated energy and the elastic energy given to the systems:

$$\zeta_e = \frac{1}{4\pi}\frac{\omega}{\Omega}\frac{\Delta E(U)}{E_e(U)} \tag{12}$$

Thus, the equivalent damping coefficient can be evaluated from the energy loss and the total energy of the system during a complete cycle.

4.3. Numerical implementation

In order to better reproduce the dissipative phenomena observed in experiments via the dynamic release test and to accurately take into account the geometry of the problem, a model based on finite element method (FEM) has been implemented. The purpose of this approach is to simulate both the evolution of the equivalent damping coefficient and the dissipated energy. The calculations were carried out using the finite element code Comsol Multiphysics (Femlab_3.2) in which the friction law described previously is integrated. The suggested model consists of a collection of Jenkins elements [22,42]. In this study, the structure is reduced in 2D (the x- and z-axes directions) with six nodes triangular elements. This choice of 2D FEM is mainly related to the presence only of the relative displacement in the x direction. The relative displacement in the y direction is wedged by the notch form manufactured in the both aluminum plates 1 and 2 (Fig. 2). In order to better simplify the 2D finite element modeling, the regularized contact law is applied only in the upper interface quartz beam. Each node of the aluminum plate ground interface is connected to quartz beam upper interface by a linear spring with an elastic stiffness in series with a Coulomb slider. The stiffness represents the capacity of the asperities to be elastically deformed. When the mechanical properties of the interface are homogeneous, the employed friction coefficient and stiffness parameter are constant along the contact interface because the surface roughness changes slightly. The stiffness parameter and the friction coefficient are then considered as global parameters of the interface. The ground quartz beam interface is jammed because the finite element contact problem became symmetric.

The tangential contact action is evaluated from a regularized version of the Coulomb law. The first modification consists in adopting a quasi-static resolution in which the velocity v_{ij} is replaced by relative displacement u_{ij} on a given time interval. The second modification consists of correcting the discontinuity of the Coulomb law in the vicinity of relative null displacements. A linear tangential force P_t evolution from the initial position until the slip threshold is used at each point of the interface between solids i and j. The evolution law is such that

$$K_t|u_{ij}| \leqslant \mu|P_n| \Rightarrow P_t = K_t|u_{ij}|\mathrm{sgn}(u_{ij}) \tag{13}$$

$$K_t|u_{ij}| \geqslant \mu|P_n| \Rightarrow P_t = \mu|P_n|\mathrm{sgn}(u_{ij}) \tag{14}$$

The use of this modeling requires defining the normal force P_n, the stiffness K_t and the Coulomb coefficient μ. In the case of a cyclic relative displacement u with an amplitude $[-U, U]$, two different situations can be distinguished. When the slip threshold is not reached, the contact behavior is purely elastic and no energy is dissipated (Figs. 10(c) and (d)). When the slip threshold is reached (Fig. 11), a classical friction behavior is assumed. For a complete period vibration, the corresponding local dissipated energy $\mathrm{d}\Delta E$ and the elastic one $\mathrm{d}E_e$ are given by the following equations:

$$\mathrm{d}\Delta E = 4\left(u - \frac{p_t}{k_t}\right)p_t\,\mathrm{d}x\,\mathrm{d}y \tag{15}$$

$$\mathrm{d}E_e = \frac{p_t^2}{2k_t}\,\mathrm{d}x\,\mathrm{d}y \tag{16}$$

where the symbol d is the infinitesimal, p_t is the tangential force par unit area, p_n is the normal force par unit area and k_t is the stiffness par unit area.

The translation of this local formulation to the global formulation of the contact is obtained by integration over the whole contact surface (ℓ and Lc, respectively, the width and the length of the clamped part of the quartz beam). Only relative displacement along the longitudinal direction (x-axis) is present in our case. The estimation of the dissipated energy corresponding to a complete vibration cycle is given by the following expression Eq. (17) [24,43], the expression of the elastic energy is given by Eq. (18) and the equivalent damping is given by Eq. (19):

$$\Delta E = 4\int_0^{Lc}\int_0^{\ell}\left|p_t\left(u - \frac{p_t}{k_t}\right)\right|\mathrm{d}x\,\mathrm{d}y = 4\int_0^{Lc}\left|\ell p_t\left(u - \frac{p_t}{k_t}\right)\right|\mathrm{d}x \tag{17}$$

$$E_e = \int_0^{Lc}\int_0^{\ell}\frac{p_t^2}{2k_t}\,\mathrm{d}x\,\mathrm{d}y = \frac{L_c\ell p_t^2}{2k_t} \tag{18}$$

$$\zeta_e = \frac{2}{\pi L_c}\frac{\omega}{\Omega}\int_0^{Lc}\left|\frac{k_t}{p_t}\left(u - \frac{p_t}{k_t}\right)\right|\mathrm{d}x \tag{19}$$

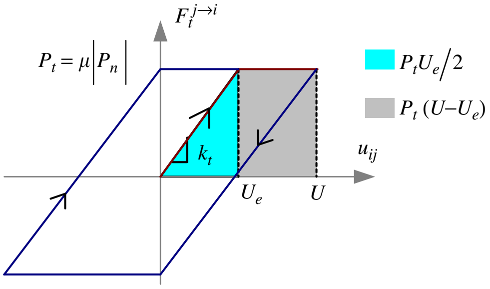

Fig. 11. Force–displacement relation of a single Jenkins element.

4.4. Parameters analysis

In order to evaluate the influence of friction parameters on microsliding, tangential friction force, dissipated energy and equivalent damping, sensitivity analysis was carried out on the model of the quartz specimen. The normal static force (constant with time) applied in order to ensure the contact is uniformly distributed on the entire contact surface ($p_n = 3.5 \times 10^5$ Pa). The vertical displacement (along z-axis) at the free part of the beam is imposed by a series of positive values between zero and the maximal deflection obtained in the experiment in order to statically deform the quartz specimen. Two sets of results are presented:

- Set (a): the friction coefficient μ is constant and the stiffness parameter varies between 3×10^{13} and $7 \times 10^{13}\,\mathrm{N\,m^{-3}}$. The corresponding results are given in Figs. 12(a), 13(a), 14(a), 15(a) and 16(a).
- Set (b): the stiffness parameter is constant and the friction coefficient μ varies between 0.1 and 0.3. The corresponding results are given in Figs. 12(b), 13(b), 14(b), 15(b) and 16(a).

Figs. 12 and 13 represent the spatial distributions along the contact interface, respectively, microsliding and contact force for the deflection of the beam free-end A_d equal to 3×10^{-6} m. Three different zones can be distinguished in Figs. 12 and 13. The first zone corresponds to the adherence (negligible microsliding (8×10^{-16} m)) and is spread on a long part of 5×10^{-6} m (70 percent of contact surface). The second zone is a transition zone characterized by the presence of partial microsliding. The microsliding values vary between 8×10^{-16} and 3×10^{-9} m on a contact distance of 1.7×10^{-3} m, equivalent to 23 percent of the contact surface. The last zone corresponds to the presence of total sliding under a constant friction or tangential force μp_n (total microsliding). It is distributed on a contact distance smaller than the two first parts and equal to

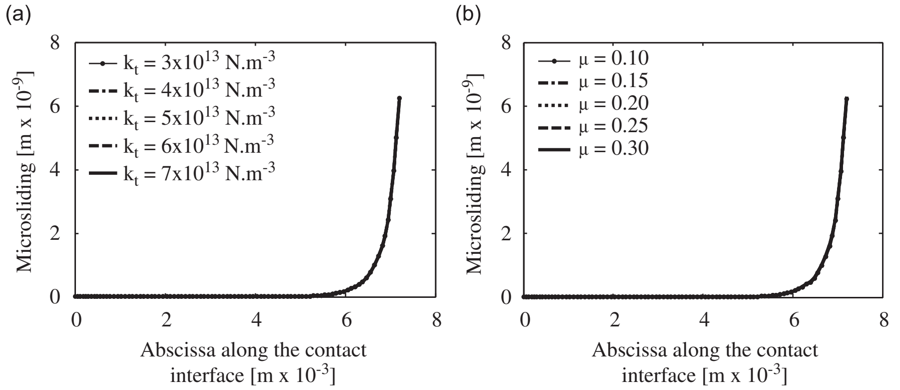

Fig. 12. Spatial microsliding repartition: (a) $\mu = 0.10$ and (b) $k_t = 5 \times 10^{13}\,\mathrm{N\,m^{-3}}$.

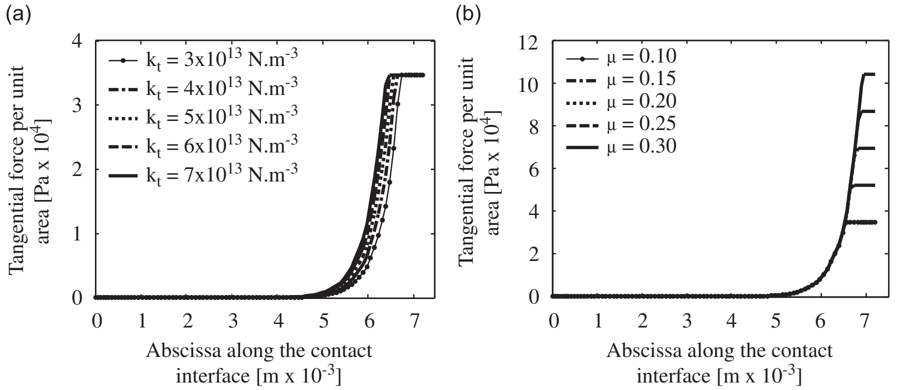

Fig. 13. Spatial contact pressure repartition: (a) $\mu = 0.10$ and (b) $k_t = 5 \times 10^{13}\,\mathrm{N\,m^{-3}}$.

0.5×10^{-3} m, equivalent to 7 percent of the surface of contact. The influences of both stiffness coefficient and friction coefficient on the microsliding are negligible (Fig. 12). The influence of the stiffness coefficient on the contact force p_t is clearly visible when magnifying the right part of the contact surface (Fig. 14(a)). The spatial evolutions of the contact force are similar, but the length of the transition zone decreases when stiffness parameter increases. The friction coefficient variation influences the contact force saturation levels and the length of the third zone (Fig. 14(b)).

The dissipated energy evolution and the equivalent modal damping evolutions are plotted according to the dynamic deflection of the beam free-end in Figs. 15 and 16. The dissipated energy values are nulls when only adherence exists over contact surface (first regime) and tend to increase proportionally to the dynamic deflection amplitude when partial microsliding exist (second regime). The third regime is also characterized by linear energy evolutions, but with higher slopes. The change of both stiffness (Fig. 15(a)) and friction coefficient (Fig. 15(b)) coefficients generate variations on the three parts of the dissipated energy evolution.

The evolutions of the equivalent modal damping (Fig. 16) show a rapid increase until their maximum value in the second regime. For larger deflections, equivalent modal damping decreases slowly versus the vibration amplitude (third regime). The variation of the stiffness parameter generates visible variations on equivalent modal damping evolution (Fig. 16(a)). The maximum value of equivalent damping goes from 1.21 to 2.93 percent when the stiffness parameter increases from 3×10^{13} to $7 \times 10^{13}\,\mathrm{N\,m^{-3}}$, which means that the quality factor becomes lower for high stiffness parameters. The maximum remains constant when the friction coefficient increases (Fig. 16(b)).

As a conclusion of the parameter analysis, the equivalent modal damping is sensitive to both friction coefficient and stiffness parameter. Therefore, model updating has a good chance to converge and thus allows the identification on the experimental parameters.

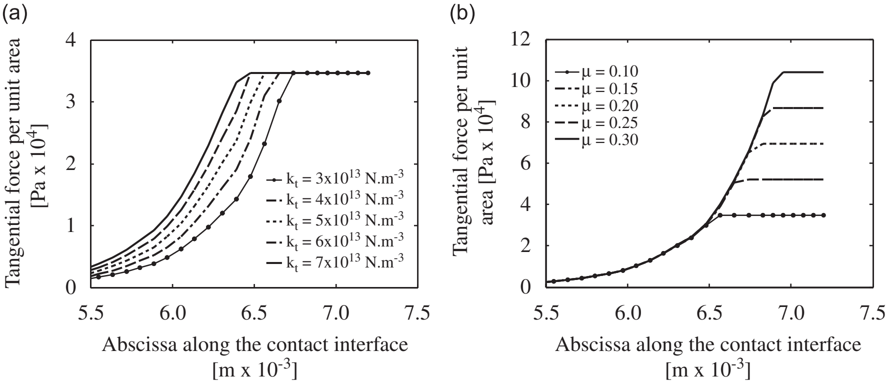

Fig. 14. Spatial contact pressure repartition: (a) $\mu = 0.10$ and (b) $k_t = 5 \times 10^{13}\,\mathrm{N\,m^{-3}}$.

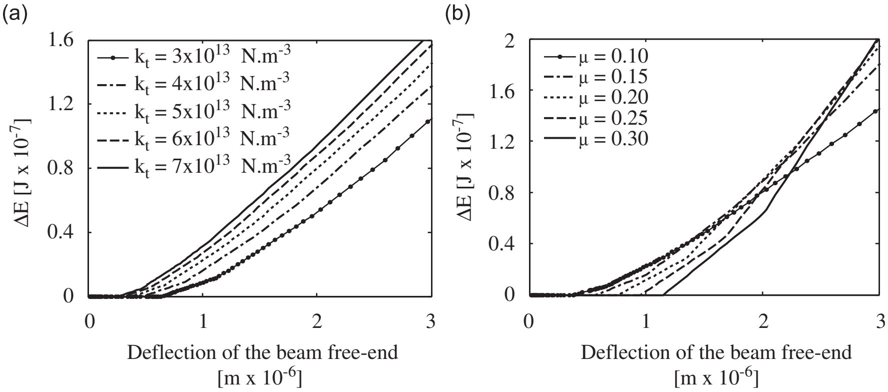

Fig. 15. Dissipated energies: (a) $\mu = 0.10$ and (b) $k_t = 5 \times 10^{13}\,\mathrm{N\,m^{-3}}$.

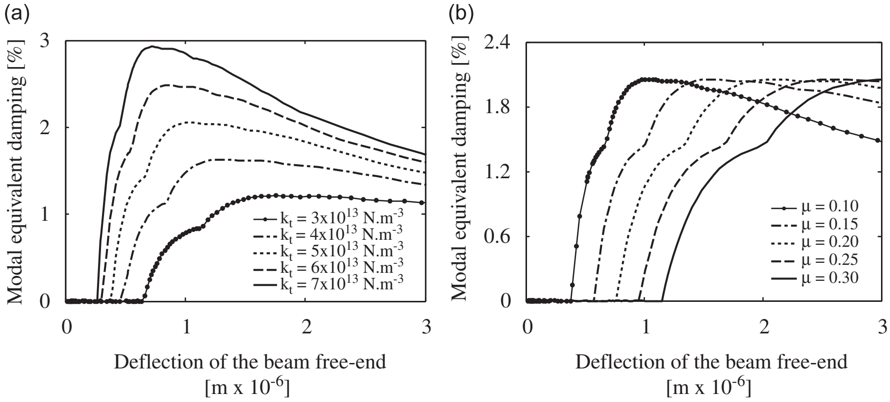

Fig. 16. Equivalent modal damping: (a) $\mu = 0.10$ and (b) $k_t = 5 \times 10^{13}\,\mathrm{N\,m^{-3}}$.

5. Identification procedure

5.1. Optimization technique

The optimization algorithm used in this study is based on the use of GAs, which were introduced by Holland and improved by Goldberg [44,45], who made them well known. GAs become widely used in mechanical problems nowadays. They imitate natural behavior in terms of biological evolution in order to reach the best possible solution to a given problem. Weak individuals tend to die before reproducing, while the stronger ones live longer and bear many offsprings, who often inherit the qualities that will enable their parents to survive. The working principle may be summarized as follows. The initial population is generated by selecting individuals in the whole considered space. Pairs of individuals are selected from this population and the selection is based on their performances (fitness/objective function values). Each pair of individuals undergoes a reproduction mechanism to generate a new population in such a way that the preferable individuals will spread their genes with higher probability. The children replace their parents. As this proceeds, inferior attributes in the pool die out due to lack of reproduction. At the same time, strong attributes tend to combine with other strong attributes to produce children who perform better. The reproduction cycle is governed by a series of genetic operators, namely selection, recombination and mutation.

Although the GAs provide very robust properties, their main drawback is that they may suffer from a slow convergence because they use probabilistic recombination operators to control the step size and searching direction. Consequently, for real industrial problems involving expensive function evaluations, the GA-required CPU time is usually impractical even with today's computing power. Therefore, the acceleration of the optimization process by exploiting an approximate model combined with the GA and by using robust and efficient genetic operators is investigated. The algorithm architecture is organized in five steps, which are summarized in Fig. 17.

(a) The first step consists in building a database using a design of experimental procedure. Numerous techniques exist: full factorial, fractional, central composite, D-optimal, Latin-hypercube and random selection among others.
(b) An approximate model is built using the design of experimental points in order to construct an analytical relation between the design variables and the simulation responses.
(c) An optimization algorithm is used to find the optimum using the approximate model to evaluate the objective functions and constraints.
(d) The accurate simulation is used to evaluate and verify the real objective function. This new simulation result is added to the database. The database is therefore always enriched with new design points, leading to an improved approximate model.
(e) Go to step (b) until the maximum number of optimization cycles specified by the user is reached.

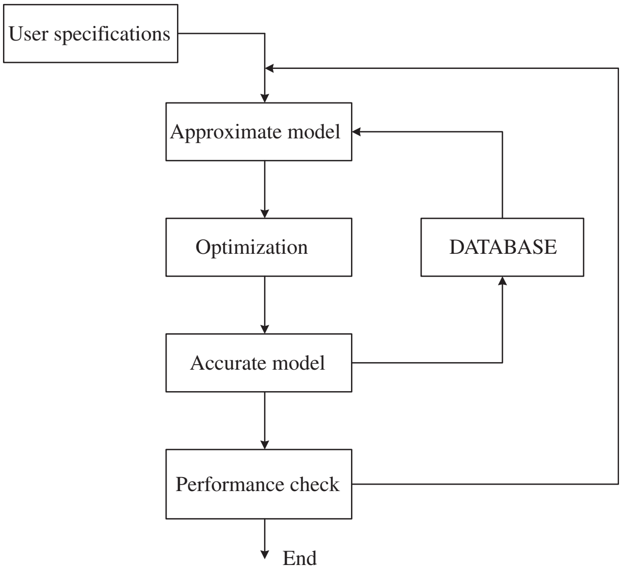

Fig. 17. Flowchart of the algorithm.

5.2. Artificial neural network

Several multidimensional and nonlinear interpolation techniques can be used to construct the approximate model, e.g. kriging, artificial neural networks (ANNs), radial basis functions or lazy learning. These techniques offer the advantages of decoupling the number of free parameters with respect to the number of design parameters, which is not the case for a simple polynomial interpolation. In this research, the back-propagation neural network is used, mainly because of its robustness in providing a more accurate model. Moreover, it allows constructing a global approximate model, suitable for the entire design space and represents an important aspect for the application of the optimization techniques. These techniques need information from the whole search space. ANNs are computational techniques, which simulate the computational abilities of biological systems. Any ANN has three principal key characteristics:

1. It consists of a number of processing elements (neurons).
2. Each neuron is connected to other elements through weighted links.
3. The functionality is determined by modifying these weights during a learning phase.

There are many types of ANN architectures in the literature. The back-propagation ANN is the most widely known and is applied here to capture preferences [46]. The back-propagation ANN is a multilayer perceptron network with a nonlinear transfer function within the neurons. The network is classified as supervised and is used in a two-stage process. The first stage is learning and the second one is prediction. During the learning process, the ANN is taught to recognize a given set of input and output conditions.

Additionally, the neurons use an enhanced transfer function, often a sigmoid, and they are usually arranged into three or more layers (see Fig. 18). Only feed forward connections are allowed and they must be between adjacent layers.

The back-propagation ANN is taught to create a mapping between input and output patterns. During the training process the input/output pairs are known. However, instead of using a delta rule (difference between input and output) a squared error rule is used. The weights are then adjusted by small amounts to reduce the error across single neurons moving backwards from the output. The adjustment of weights via this back-propagation continues until the squared error term is reduced below a certain threshold over the complete training data set. When this has been achieved the trained network can be used as a predictor giving an output pattern based on any given inputs.

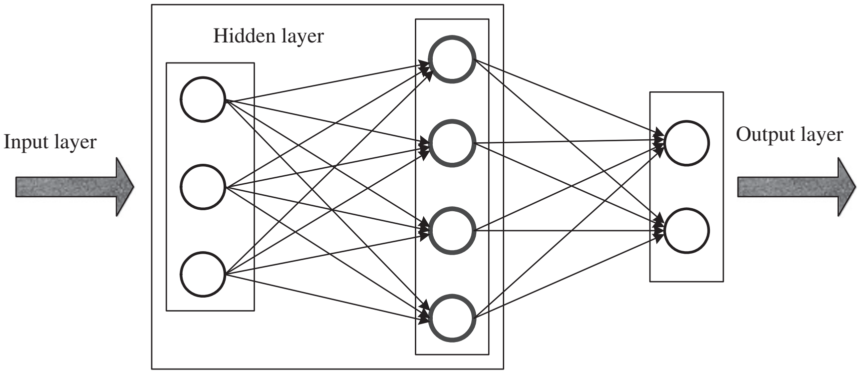

Fig. 18. Graphical illustration of multilayer perceptron network.

5.3. Model updating

This technique is developed and applied here in order to optimize both the parameter stiffness and the friction coefficient used in the finite element model with the aim of better reproducing the equivalent damping identified on the quartz specimen. The performance function used to solve this mono-objective problem is the quadratic error ψ_q between the experimental results and those given by the finite element model

$$\psi_q = \langle ||\sigma - \phi(\mu, k_t)|| \rangle \tag{20}$$

where σ denotes the experimental values of equivalent damping obtained under the primary vacuum (a high percentage of the damping caused by the ambient air presence is eliminated) and ϕ denotes the values of equivalent damping generated by the finite element model. In this modeling, the selected generation number is equal to 20. The error function between the model and the experiment converges after five generations towards a minimal error value of 0.3031 (Fig. 19). The response surface of the error evolution according to the parameters to be optimized makes it possible to provide the best set of identified coefficients: the stiffness coefficient k_t and the friction coefficient μ. Fig. 20 shows that the optimal value of the error is singular. The identified stiffness parameter and friction coefficient μ corresponding to the minimal error value are given in Table 1.

5.4. Results and discussions

The behavior of the optimized numerical model is presented in this section. First, equivalent modal damping evolutions according to the dynamic deflection amplitude of the free part of the quartz beam are shown in Fig. 21 for both the experimental and the optimized models. The numerical damping curve fits the experimental one well for the high dynamic deflection amplitude. For amplitude lower than 0.65×10^{-6} m, the simulated damping is null due to the fact that no microsliding occurs while the experimental damping varies between 0.4 and 0.9 percent. That difference comes from the fact that friction is the only energy dissipation source that is taken into account in the model, whereas the experiment is subject to other dissipative phenomena like radiation and heat transfer in the whole setup. The microsliding and the contact force p_t according to the abscissa along the contact are shown in Fig. 22. The dissipated energy evolution according to the dynamic deflection is presented in Fig. 23, and starts increasing when the dynamic amplitude is sufficient to activate microsliding processes on the interface.

Finally, the modeling correctly reproduces the experimental modal equivalent damping evolution due to dry friction, confirming that the relative microsliding in contact surfaces is the main source of damping in small structures clamped by the bolts. The computed relative microsliding and contact force p_t provide information on the most critical places for energy losses in the case of this kind of connection.

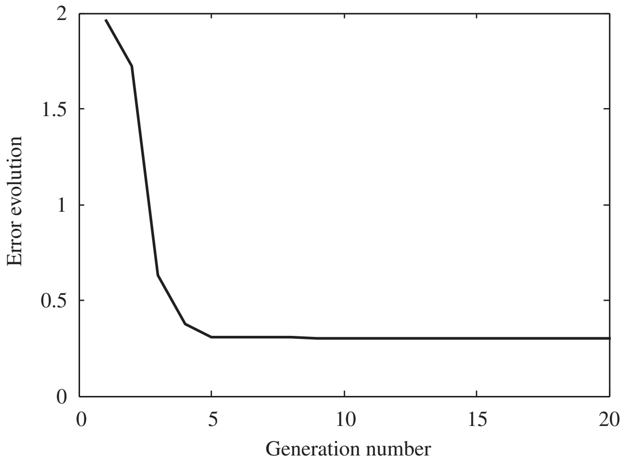

Fig. 19. Response function (error) versus the number of generations.

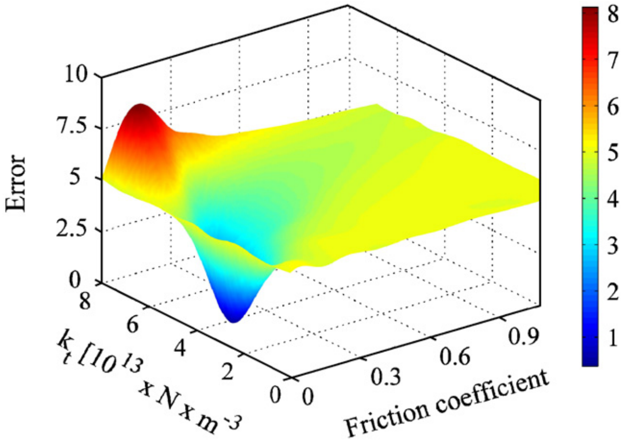

Fig. 20. Response surface evolution versus the optimized parameters (k_t and μ).

Table 1
Identified parameters

Stiffness parameter, k_t ($\mathrm{N\,m^{-3}}$)	3.8×10^{13}
Coefficient of friction, μ	0.165

6. Conclusion

In this paper, the damping produced in the clamped part of small cantilever quartz beam is studied both experimentally and numerically.

The experimental identification was performed using a technique based on the wavelet transform of free responses obtained from dynamic release tests. The evolution of the equivalent damping versus the dynamic deflection of the beam reveals a nonlinear behavior typically associated to the stick-slip phenomenon.

A finite element implementation of the regularized Coulomb law was performed. Stiffness and friction parameters were updated thanks to an optimization procedure based on a genetic algorithm combined with an artificial neural network. A good agreement between numerical and experimental results was achieved. The

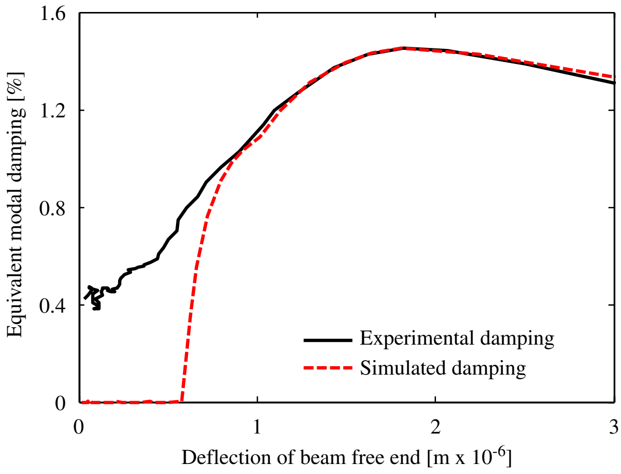

Fig. 21. Confrontation of optimized equivalent damping and experimental equivalent damping.

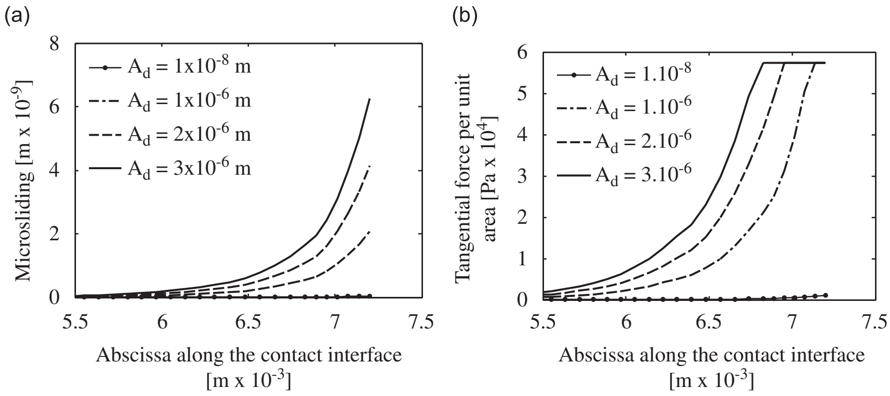

Fig. 22. (a) Spatial microsliding repartition and (b) spatial contact pressure repartition.

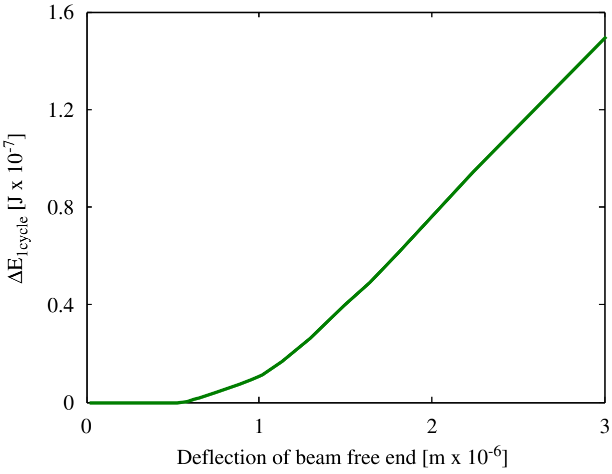

Fig. 23. Optimized dissipated energy.

finite element model brings interesting additional information: the spatial distribution of microsliding and tangential force along the contact interface. It appears that these distributions are strongly non-uniform, and that most of the damping is produced in the region, which separates the clamped part from the free part of the quartz beam.

The significant values of the damping also indicate that other assembly techniques like anodic bonding should be preferable in the case of small size systems used for energy scavenging.

Acknowledgments

This work is financed, on the one hand, by the European Commission through the project STREP VIBES (IST-1-507911) (Vibration Energy Scavenging) for the 6th programme and on the other hand, by Joint action Energy of CNRS & Research Ministry.

References

[1] S. Roundy, P.K. Wright, J.M. Rabaey, A study of low level vibrations as a power source for wireless sensor nodes, *Computer Communications* 26 (2003) 1131–1144.

[2] E. Lefeuvre, A. Badel, C. Richard, L. Petit, D. Guyomar, A comparison between several vibration-powered piezoelectric generators for standalone systems, *Sensors and Actuators A* 126 (2006) 405–416.

[3] G. Poulin, E. Sarraute, F. Costa, Generation of electrical energy for portable devices, comparative study of an electromagnetic and a piezoelectric system, *Sensors and Actuators A* 116 (2004) 461–471.

[4] R. Dakhlaoui, A. Baczmański, C. Braham, S. Wroński, K. Wierzbanowski, E.C. Oliver, Effect of residual stresses on individual phase mechanical properties of austeno-ferritic duplex stainless steel, *Acta Materialia* 54 (2006) 5027–5039.

[5] R. Dakhlaoui, C. Braham, A. Baczmański, Mechanical properties of phases in austeno-ferritic duplex stainless steel—surface stresses studied by X-ray diffraction, *Materials Science and Engineering A* 444 (2007) 6–17.

[6] F.R. Blom, S. Bouwstra, M. Elwenspoek, J.H.J. Fluitman, Dependence of the quality factor of micromachined silicon beam resonators on pressure and geometry, *Journal of Vacuum Science and Technology B* 10 (1992) 19–26.

[7] S.D. Panteliou, T.G. Chondros, V.C. Argyrakis, Damping factor as an indicator of crack severity, *Journal of Sound and Vibration* 241 (1999) 235–245.

[8] R. Lifshitz, M.L. Roukes, Thermoelastic damping in micro- and nanomechanical systems, *Physical Review B* 61 (2000) 5600–5609.

[9] H. Hosaka, K. Itao, S. Kuroda, Damping characteristics of beam-shaped micro-oscillators, *Sensors and Actuators A* 49 (1995) 87–95.

[10] H. Hosaka, Y. Uenishi, Static rigidity and natural frequency of flat permalloy springs used in electromagnetic microactuators, *International Journal of the Japan Society for Precision Engineering* 27 (1993) 253–258.

[11] H. Nouira, E. Foltête, L. Hirsinger, S. Ballandras, Investigation of the effects of air on the dynamic behavior of a small cantilever beam, *Journal of Sound and Vibration* 350 (2006) 243–260.

[12] H. Nouira, E. Foltete, L. Hirsinger, S. Ballandras, Investigation of air effect on the resonance frequency and damping of three small assembled structures by different adhesive materials (SU8 epoxy resin and compressed gold): Smart materials and structures, 17 (2008) 035016 (11pp).

[13] G.S. Kino, *Acoustic Waves: Devices, Imaging, and Analog Signal Processing*, Prentice-Hall, Englewood Cliffs, NJ, 1987.

[14] P.W. O'Callaghan, S.D. Probert, Prediction and measurement of true areas of contact between solids, *Wear* 120 (1987) 29–49.

[15] J.A. Greenwood, in: I.L. Singer, H.M. Pollock (Eds.), *Contact of Rough Surfaces, Fundamentals of Friction: Macroscopic and Microscopic Processes*, Kluwer Academic Publishers, The Netherlands, 1992, pp. 37–54.

[16] D. François, A. Pineau, A. Zaoui, *Comportement mécaniques des matériaux*, Hermès, Paris, 1995.

[17] L.E. Goodman, J.H. Klumpp, Analysis of slip damping with reference to turbine-blade vibration, *Journal of Applied Mechanics* (1956) 421–429.

[18] J.C. Heald, Deployment repeatability in mechanically jointed precision structures, Report CU-CAS-03-06, USA, 2003.

[19] L. Heller, Amortisement dans les structures assemblées, Ph.D. Thesis, Institut de FEMTO, Laboratory of Applied Mechanics, University of Franche Comté, Besançon, 2005.

[20] H. Olsson, H.J. Astrom, C. Canudas de Wit, M. Gafvert, P. Lischinsky, Friction models and friction compensation, *European Journal of Control*, 1998.

[21] H.J. Kleep, Trial-and-error procedure for single-degree-of-freedom systems with friction-affected sliding joints, *Journal of Sound and Vibration* 191 (1996) 598–605.

[22] W.D. Iwan, On a class of models of the yielding behavior of continuous and composite systems, *Journal of Applied Mechanics* (1967) 612–617.

[23] P. Dahl, A solid friction modelo, Technical Report TOR-0158H3107–18I-1, The Aerospace Corporation, El Segundo, CA, 1968.

[24] Y. Song, C.J. Hartwigsen, D.M. McFarland, A.F. Vakakis, L.A. Bergman, Simulation of dynamics of beam structures with bolted joints, *Journal of Sound and Vibration* 273 (2004) 249–276.

[25] U. Olofsson, Cyclic microslip under unlubricated conditions, *Tribology International* 28 (1995) 207–217.

[26] L. Ratton, T. Kunt, T. Mc. Avoy, T. Fuja, R. Cavicchi, S. Semancik, A comparative study of signal processing techniques for clustering microsensor data (a first step towards an artificial nose), *Sensors and Actuators B* 41 (1997) 105–120.

[27] S. Mallat, Une exploitation des signaux en ondelettes, Les éditions de l'Ecole Polytechnique, Paris, Juillet 2000.

[28] J. Slavic, I. Simonovski, M. Boltezar, Damping identification using a continuous wavelet transform: application to real data, *Journal of Sound and Vibration* 262 (2003) 291–307.

[29] J. Lardies, M.-N. Ta, M. Berthillier, Modal parameter estimation based on the wavelet transform of output data, *Archive of Applied Mechanics* 73 (2004) 718–733.

[30] W. Ling, A hybrid genetic algorithm-neural network strategy for simulation optimization, *Journal of Applied Mathematics and Computation* 170 (2005) 1.

[31] B. Ait Brik, Méthodologies de conception robuste et d'optimisation dans un contexte de conception d'architectures mécaniques nouvelles en avant projet, Ph.D. Thesis, Institut de FEMTO, Laboratory of Applied Mechanics, University of Franche Comté, Besançon, 2005.

[32] J. Lardies, S. Gouttebroze, Identification of modal parameters using the wavelet transform, *International Journal of Mechanical Sciences* 44 (2002) 2263–2283.

[33] M.N. Ta, J. Lardies, Identification of weak non-linearities on damping and stiffness by the continuous wavelet transform, *Journal of Sound and Vibration* 293 (2006) 16–37.

[34] Z. Osinski (Ed.), *Damping of Vibrations*, A.A. Balkema, Rotterdam, Brookfield, 1998.

[35] T.P. Le, Auscultation dynamique des structures à l'aide de l'analyse continue en ondelettes, Ph.D. Thesis, Ecole Nationale des Ponts et Chaussées, France, 2005.

[36] F.P. Bowden, D. Tabor, *The Friction and Lubrication of Solids*, Oxford University Press, Oxford, 1950.

[37] F.P. Bowden, D. Tabor, *The Friction and Lubrication of Solids, Part II*, Oxford University Press, Oxford, 1964.

[38] H.C. Wong, N. Umehara, K. Kato, The effect of surface roughness on friction of ceramics sliding in water, *Wear* 218 (1998) 237–243.

[39] L.S. Jacobsen, Steady forced vibration as influenced by damping, *Transactions ASME* 52 (1930) 169–181.

[40] W.T. Thomson, *Vibration Theory and Applications*, Prentice-Hall, Englewood Cliffs, NJ, 1965.

[41] S.S. Rao, *Mechanical Vibrations*, Addison-Wesley, Reading, MA, 1990.

[42] D.J. Segalman, An initial overview of Iwan modeling for mechanical joints, Sandia Report SAND2001-0811, USA, 2001.

[43] H. Nouira, E. Foltête, L. Hirsinger, S. Ballandras, Experimental evidence and modeling of microsliding on cantilever quartz beam, *IEEE Ultrasonics Symposium* (2007) 195–199.

[44] A.C. Keys, L.P. Rees, A.G. Greenwood, Performance measures for selection of metamodels to be used in simulation optimization, *Decision Sciences* 33 (2002) 31–57.

[45] D.E. Goldberg, *Genetic Algorithms*, Addison Wesley, Reading, MA, 1994.

[46] J. Lawrence, *Introduction to Neural Networks: Design, Theory, and Applications*, California Scientific Software, Nevada City, CA, 1993.